Microsystems & Nanoengineering
www.nature.com/micronano

ARTICLE Open Access

Single-cell impedance sensing on integrated circuit chip for fast tumor diagnosis

Wenhao Hui[1,2,3], Lang Chen[4], Stephanie Andaluz[1,2,5], Yunlong Zhong[6], Xinru Huang[7], Ren Shen[1,2], Zhen Zhu[8], Hanbin Ma[9,10], Pui-In Mak[1,2], Rui Martins[1,2,11], Ping Wang[6]✉, Shuhong Yi[7]✉, Wei Wang[4]✉, Ka-Meng Lei[1,2]✉ and Yanwei Jia[1,2,12]✉

Abstract

Accurate and prompt tumor diagnosis plays a critical role in surgical decision-making to minimize damage to patients with benign tumors and maximize the cure rate of cancer patients. Although imaging, molecular testing, and histopathology assist in preoperative and postoperative tumor assessments, a fast, automated, and easy-to-operate method for intraoperative tumor diagnosis is lacking. Here, we introduce an innovative integrated circuit-based single-cell electric cell-substrate impedance sensing (IC-ECIS) platform capable of rapid intraoperative differentiation between cancerous and non-cancerous tumors. Fabricated on a semiconductor chip, this system captures ultra-weak single-cell impedance signals with exceptional sensitivity for single-cell discrimination for cancer risk evaluation. The implementation of a polymer-embedded silicon fan-out (P-eSiFO) packaging approach has reduced post-fabrication costs to under $1 per chip and allowed the microelectrodes batch processing on multi-project wafer chips. The diagnostic results can be obtained in 20 min without compromising cell viability. Clinical tumor samples from the thyroid, liver, gallbladder, bile duct, breast, and pancreas were tested on-chip to evaluate cancer risk. The on-chip diagnostic findings aligned with traditional histopathological analysis and flow cytometry results. This technology provides a fast, stable, automated, and low-sample-consumption diagnostic solution for tumors, paving the way for large-scale implementation of semiconductor-based diagnostic tools in precision oncology and personalized medicine.

Diagnosis of a tumor to be benign, precancerous, or cancerous is critical for choosing the most appropriate treatment[1–3]. While many benign tumors do not need surgical resection, some do, especially those causing symptoms. Whenever possible, minimally invasive techniques with small incisions and minimal recovery times are used for benign tumor resection. But the treatment for malignant tumors requires more aggressive surgical procedures. The entire tumor mass, as well as enough healthy tissue around it, should be removed to minimize the chance of cancer recurrence[4,5]. Misdiagnosis of a tumor may result in either inadequate resection, leaving malignant cells behind, initiating recurrence of the tumor, or excessive resection, causing unnecessary damage to the organ. At present, imaging methods (such as ultrasound, computed tomography (CT), magnetic resonance imaging, and positron emission tomography-computed tomography) and molecular biology tests (such as tumor markers) are commonly used in clinical practice for the early evaluation of tumors[6,7]. However, imaging methods have a higher false negative rate when detecting small-volume lesions (< 8 mm). Molecular biomarkers exhibit high specificity, but their levels often rise significantly only at advanced disease stages or under high tumor burden, which limits their reliability for early-stage cancer detection[8]. In most situations, removing tissue and studying it

Correspondence: Ping Wang (wangping1219@126.com) or Shuhong Yi (yishuhong@163.com) or Wei Wang (w.wang@pku.edu.cn) or Ka-Meng Lei (kamenglei@um.edu.mo) or Yanwei Jia (yanweijia@um.edu.mo)
[1]State Key Laboratory of Analog and Mixed-Signal VLSI, Institute of Microelectronics, University of Macau, Macau, SAR, China
[2]Faculty of Science and Technology, University of Macau, Macau, SAR, China
Full list of author information is available at the end of the article
These authors contributed equally: Wenhao Hui, Lang Chen

is the only way to diagnose cancer definitively. In clinical settings, the gold standard tumor diagnosis method is based on formalin-fixed paraffin embedding, which preserves and prepares biopsy samples for examination of tissue architecture, cellular morphology, capsular integrity, and vascular invasion to differentiate benign tumors from malignant ones[9]. This time-consuming process of fixation, embedding, sectioning, and staining typically takes about one week, rendering it unsuitable for real-time guidance of surgical resection margins[10]. For rapid analysis of tissue samples in real time, frozen section analysi was introduced as a fast diagnostic method, providing preliminary results within 1 hour[11]. Despite its rapid turnaround, the procedure is technically demanding, with an accuracy of 85–90% that depends strongly on slide quality, staining reagents, and the pathologist's expertise[12]. Additionally, preparing frozen sections is challenging because of the small number of biopsy samples or calcified tissues. In certain tumor types, such as thyroid follicular tumors, the integrity of the capsule and blood vessels may not be clearly visible in frozen sections, increasing the risk of misdiagnosis[13].

To address this issue, several emerging technologies have shown promise in the field of fast tumor diagnosis. Flow cytometry enables tumor cell detection and classification by analyzing multiparametric fluorescence signals generated from laser-excited, antigen-specific antibodies bound to cellular markers[14]. However, it relies on predefined antigen panels, which may miss tumors lacking specific markers, such as undifferentiated carcinomas or rare subtypes. The high cost of equipment/maintenance also limits its accessibility in resource-limited clinical settings[15]. To improve the universality, Johan et al. applied digital pathology scanning technology to convert tissue samples into high-resolution digital images and employed deep learning algorithms for tumor property analysis[16]. Artificial intelligence (AI)-assisted diagnosis has demonstrated comparable accuracy to pathologists in detecting breast and liver tumors, offering advantages in detecting small lesions[16,17]. While this method enhances accuracy, it still depends on the conventional pathology of slices, and preprocessing remains complex and takes several hours. To simplify sample preparation protocols, Wijsman et al. introduced optical coherence tomography (OCT), a high-resolution non-invasive imaging technique that provides real-time tissue microstructure information for intraoperative tumor boundary assessment and preliminary identification of benign and malignant tumors[18]. Although OCT provides real-time microstructural information, its penetration depth is limited to 2–3 mm, restricting its application to non-transparent or highly scattered solid tumor tissues[19]. In parallel, emerging label-free optical and molecular techniques have been explored for rapid intraoperative tumor diagnosis. Stimulated Raman histology enables near-real-time generation of histology-like images from fresh tissue without staining and has shown promising performance when combined with AI[20], while intraoperative mass spectrometry–based approaches, such as the MasSpec Pen and rapid evaporative ionization mass spectrometry, provide real-time tissue identification based on molecular fingerprints[21,22]. However, these techniques typically rely on specialized and costly instrumentation, intact tissue specimens, or complex intraoperative workflows, which may limit their routine clinical deployment[23].

Electric cell-substrate impedance sensing (ECIS) is a label-free and non-invasive technique that characterizes cell behaviors by monitoring impedance variations at the cell–electrode interface, and has been widely used to study cell adhesion, spreading, and barrier properties in real time[24,25]. Beyond the classical ECIS configuration with small planar electrodes, interdigitated microelectrodes (IDEs) with microscale finger–gap patterns have been extensively adopted to enhance impedance sensitivity for detecting cell attachment by enlarging the effective electrode–cell interaction area[26]. In addition, ECIS platforms based on microelectrode arrays enable parallel or spatially resolved impedance measurements, allowing statistical analysis of cell populations rather than single sensing sites[27]. Despite these advances, conventional ECIS approaches exhibit inherent limitations when applied to primary clinical samples, particularly in scenarios involving low cell numbers and heterogeneous cell populations[27]. In such cases, impedance signals from individual or sparse cells are often comparable to the background noise level, and overlapping impedance distributions from different cell types can hinder reliable discrimination[27]. A major contributing factor is that traditional ECIS systems typically rely on external impedance analyzers and long electrical interconnections between electrodes and peripheral readout circuits, which introduce parasitic capacitance, environmental interference, and thermal noise that degrade signal fidelity[27].

In this study, we propose an advanced method for fast tumor diagnosis based on single-cell electric cell-substrate impedance sensing on an integrated circuit (IC) chip. Figure 1 illustrates the schematics of the diagnostic process. Tumor biopsy samples are dissociated into single cells and loaded on a semiconductor chip for impedance measurement. The IC right under the surface electrodes for electric cell-substrate impedance sensing maximizes the signal-to-noise ratio to distinguish cancer cells from non-cancerous cells at the single-cell level. The microelectrode array integrated on the chip is highly scalable and offers high throughput. The proportion of cancer cells in a biopsy sample indicates the risk level of the tumor being benign or malignant. The whole process, from sample acquisition to turnaround, can be achieved

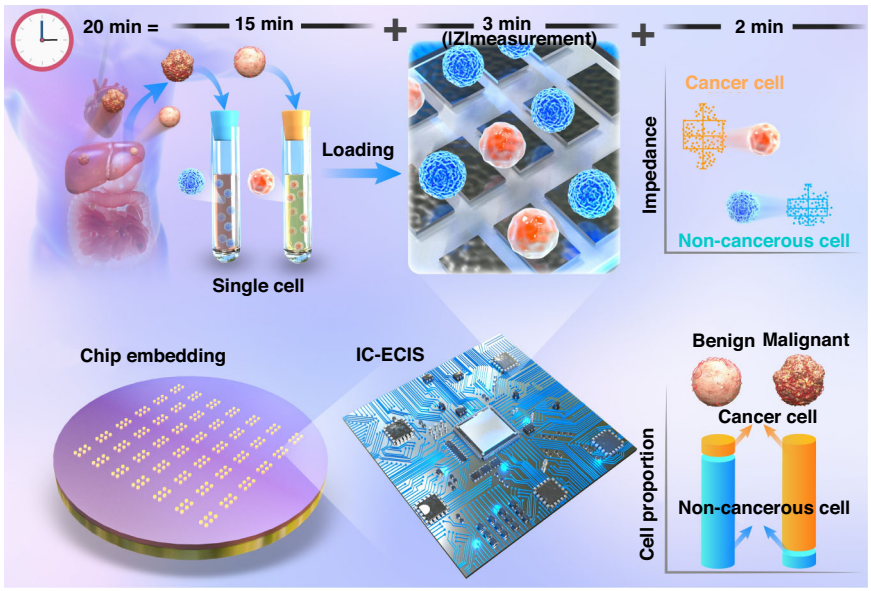

Fig. 1 Schematics of the integrated circuit-based electric cell-substrate impedance sensing (IC-ECIS) for tumor diagnosis. Schematic overview of the IC-ECIS workfl ow for rapid intraoperative tumor diagnosis, showing tumor sample dissociation into single cells, loading onto the integrated circuit chip for impedance measurement, and cancer risk classification based on single-cell impedance analysis

in 20 min. Moreover, we innovatively introduce a polymer-based embedded silicon fan-out (P-eSiFO) technique for the fabrication of surface electrodes on massive amounts of IC chips in one batch, greatly increasing the throughput of chip post-processing. We have applied the IC-ECIS to clinical tumors from various organs, including the thyroid, liver, gallbladder, bile duct, breast, and pancreas. The diagnostic results were consistent with the hospital pathology and flow cytometry results. The turnaround time of <30 min makes IC-ECIS a promising platform for effective tumor diagnosis during surgery.

Results and discussion

IC-based electric cell-substrate impedance sensing (IC-ECIS) system

ECIS has been widely used to distinguish cancer cells from non-cancerous cells[28,29]. However, a big population of cells (~ 10^5 cells) is needed to generate distinguishable impedance signals to overcome the noise generated by the connections between the sensing electrodes and the peripheral detection circuits. For discrimination between cancer and non-cancerous cells at the single-cell level, we developed a semiconductor chip with cell-sized surface electrodes for cell adhesion and ICs right beneath the sensing electrodes for signal amplification to reduce electrical noise and, therefore, improve the signal-to-noise ratio. The sensing system is named the IC-based single-cell electric cell-substrate impedance sensing (IC-ECIS) platform.

Figure 2a depicts the layout of the IC-ECIS platform, which consists of four main components: an IC chip with peripheral circuits, a signal generator, an analog-to-digital converter for acquiring waveforms at the chip output, and a field-programmable gate array (FPGA) for storing and analyzing impedance data. The sensing IC chip features impedance detection and amplification circuits to acquire impedance across the selected electrodes within the 22 × 16 electrode array. The connection pads on the IC are connected to peripheral circuitry with gold wires, facilitating low-noise communication and data transfer. The row and column control modules activate specific electrode channels within the array, routing the captured signals to a set of sixteen transimpedance amplifiers (TIA), each of which is responsible for processing the signals from one row of electrodes. The transimpedance gain of the TIA is digitally programmable to accommodate different cell types as well as excitation amplitudes. The detailed simulation results are shown in the Electronic Supplementary Information (ESI) (Figure. S1). Moreover, the TIA is biased with a constant transconductance biasing circuit to stabilize the transimpedance gain across the temperature range of interest, thereby safeguarding the operation robustness amid environmental variations. After the cell mixture is loaded onto the chip, the precise locations of individual cells are identified under a microscope. The signal generator delivers sinusoidal excitation to the IC chip, activating the relevant electrode channel. The FPGA controls and processes the data by sending digital signals to the chip,

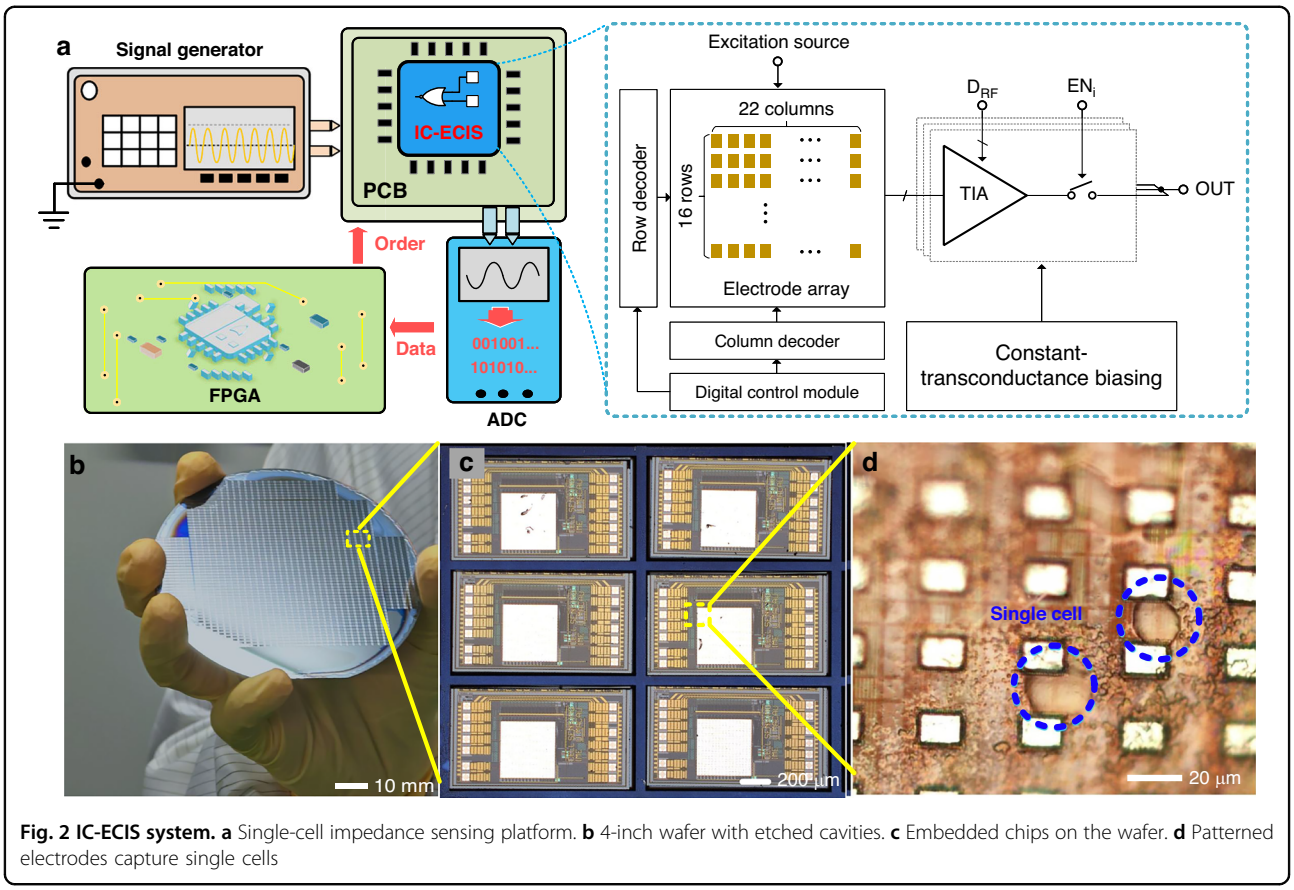

Fig. 2 IC-ECIS system. a Single-cell impedance sensing platform. **b** 4-inch wafer with etched cavities. **c** Embedded chips on the wafer. **d** Patterned electrodes capture single cells

engaging specific rows and columns of electrodes for measurement. This configuration ensures reliable detection of ultra-weak electrical signals and real-time processing, thereby enhancing the system's efficiency and automation.

With the conventional IC manufacturing process, the entire top surface of the chip is metal, which needs post-processing to fabricate electrodes of size 10 μm × 20 μm on a chip of size 1 mm × 2 mm. Although the focused ion beam technique can cast precise electrodes on an IC chip[30], the cost prevents mass production. For high-throughput surface electrode fabrication, we embedded multiple IC chips into a silicon wafer, borrowing the polymer-embedded silicon fan-out (P-eSiFO) technique[31]. The grooves were accurately etched via a mature silicon etching process. Then, the IC chips were embedded in the grooves on the silicon substrate with gaps between the chips and the sidewalls of the grooves filled with a polymer adhesive[31,32]. The mature lithography technique was subsequently utilized to cast micro-sized electrodes on

The surface of the IC chips in batches for mass production

In practice, the maximum number of chips that can be processed at once depends on the wafer size. The number of chips per wafer (CPW) estimates the cuttable grains, as shown in Eq. (1)[33].

$$CPW = \frac{\pi \times \left(\frac{d}{2}\right)^2}{W \times L} - \frac{\pi \times d}{\sqrt{2 \times W \times L}} \quad (1)$$

where d is the diameter of the wafer, W represents the width of the chip, and L is the length of the chip. The impedance sensing chip in this work had dimensions of 2152 × 1212 μm. To fit the precision of the dicing saw, a 300 μm wide scratch line was included. On a 4-inch wafer, a maximum of 2360 chips can be accommodated, as shown in Fig. 2b, ensuring high-throughput fabrication of the sensing chips under laboratory conditions.

With a cavity design that matches the shape and thickness of the IC chip, with a chip and a chip edge trench of 6 μm, the chips were securely embedded in a silicon wafer. We used parylene C to fill the gap between the embedded chip and the silicon adapter plate, given its biocompatibility, electrical insulation, and chemical inertness. As shown in Fig. 2c, the IC chips were tightly arranged with a height difference between the buried chip and the silicon substrate of <1 μm. The precise and robust fabrication of the embedded chip benefited subsequent high-precision lithography. More processing details can be found in the ESI.

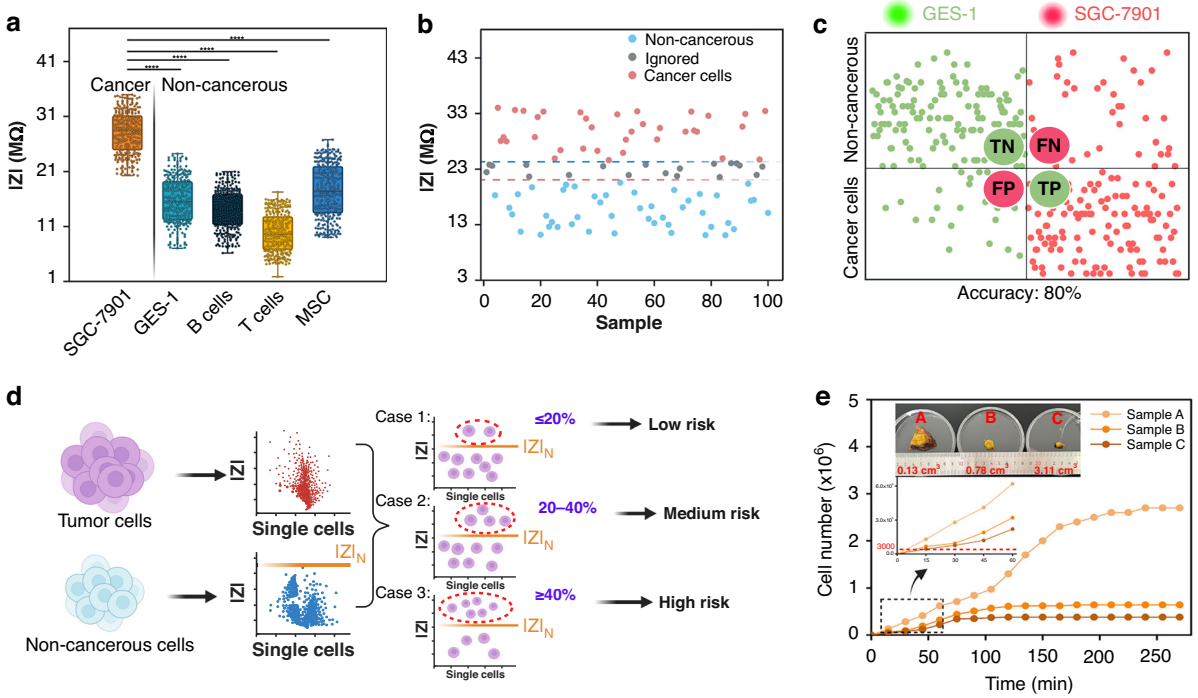

Fig. 3 Validation of the single-cell classification method based on IC-ECIS. a Impedance magnitude of human gastric cancer cell line (SGC-7901) and the corresponding gastric epithelial cell line (GES-1), B lymphocytes, T lymphocytes, and mesenchymal stem cells (MSCs). **b** Single-cell classifier based on impedance magnitude. **c** Impedance differentiation map of mixed stained cell samples (GES-1 and SGC-7901). **d** A cancer risk evaluation criterion based on impedance sensing. **e** The number of single cells dissociated from tumors of different sizes

During our IC fabrication, a 925 nm thick metal layer, consisting of 95% aluminum and 5% copper, was exposed at the sensing region following the tape-out stage. To increase the compatibility of the metal electrode with cells for good adhesion, a layer of platinum was deposited atop the preexisting metal. Ion beam etching was applied to remove excess metals, allowing for the creation of patterned electrodes without destroying the ICs underneath, which are essential for impedance sensing and signal amplification. The electrode array after etching, depicted in Fig. 2d, shows a uniform and neatly arranged pattern meeting the requirements for single-cell impedance measurements.

IC-ECIS for distinction of commercial cancer and non-cancerous cells

To evaluate the performance of the IC-ECIS system for distinguishing cancer cells from non-cancerous cells in a biopsy sample at the single-cell level, we chose a commercial human gastric cancer cell line (SGC-7901) as the model cancer cell line and a gastric epithelial cell line (GES-1) as the corresponding non-cancerous cell line for investigation. Non-cancerous cells, including immune cells (B lymphocytes and T lymphocytes), which may be present in tumor tissue, and mesenchymal stem cells (MSCs), which are sometimes used in cancer therapy, were also investigated for accuracy evaluation. The impedance magnitude between two adjacent electrodes loaded with a single cell was measured for comparison.

As illustrated in Fig. 3a, compared with all four types of non-cancerous cells, cancer cells demonstrated a significantly greater magnitude of impedance[34]. The higher impedance of cancer cells (SGC-7901) than non-cancerous tissue cells (GES-1) may be due to the unique physical properties and metabolic activities of cancer cells[35]. As cells transition into a cancerous state, they undergo significant changes in transmembrane potential, surface charge, ion concentration, etc[36]. Cancer cells tend to release higher quantities of lactate ions, which can cross the cytoplasmic membrane, leading to a substantial buildup of negative charges on the cell membrane surface[37,38]. When applied to an electric field, this accumulated negative charge can generate a current in the opposite direction, thereby enhancing the impedance[39]. Moreover, cancer cells express more proteins related to adhesion, migration, and invasion[40,41]. When cells adhere to the electrode surface via these proteins, charge transfer becomes more challenging, as they must pass through a layer of non-conductive extracellular adhesion protein, leading to an increase in charge transfer resistance[42]. Both mechanisms could cause an increase in the impedance amplitude of cancer cells compared with that of non-cancerous or precancerous

cells. The reluctance of immune cells to adhere to electrodes results in their low impedance[43]. Among the non-cancer cells, T cells had the lowest impedance magnitude, which is also attributed to their smaller size[44]. MSCs had a lower impedance than cancer cells, but slightly higher compared with the immune cells. This may be due to the complicated differentiation states of the MSCs, which cause the overexpression of certain proteins[45,46].

To build a criterion for the reliable discrimination of a single cancer cell from a non-cancerous cell, we carefully studied the range of their impedances. Considering that MSCs seldom appear in a biopsy sample, only normal tissue cells and immune cells were analyzed. As shown in Fig. 3b, the impedance magnitude of non-cancerous gastric cells ranged from 7 to 24 MΩ, whereas that of gastric cancer cells ranged from 21 to 35 MΩ. Cells with impedance magnitudes in the range of 21 to 24 MΩ could not be definitively determined due to cancer cell morphological heterogeneity and potential impedance overlap caused by size variation. These data were excluded from the analysis. However, cells with impedance magnitudes above the upper limit of non-cancer cells (24 MΩ) were most likely to be cancerous, whereas those with impedance magnitudes below the lower limit of cancer cells (21 MΩ) were most likely to be normal. To account for cancer cell morphological heterogeneity and potential impedance overlap caused by size variation, our platform does not rely on single-cell absolute impedance values but instead applies a statistical classification based on impedance distribution ranges, with ambiguous intervals excluded from decision-making to emphasize intrinsic dielectric and adhesion-related differences.

To evaluate the accuracy of the cell classification based on IC-ECIS, we labeled SGC-7901 and GES-1 cells with red and green fluorescence, respectively, for biochemical cell identification. The labeled cells were then classified as cancer or non-cancerous cells via IC-ECIS according to the above criteria. The impedance differentiation map is shown in Fig. 3c. The classification was accurate for the samples in the second and fourth quadrants, where GES-1 cells were correctly identified as non-cancerous cells, while SGC-7901 cells were identified as cancer cells. Those in the first and third quadrants were misidentified. The accuracy of the classifier model is defined as:

$$ACC = \frac{TN + TP}{TN + FN + TP + FP} \quad (2)$$

where true negative (TN) indicates cells correctly identified as non-cancerous that are indeed non-cancerous, whereas false negative (FN) refers to cells incorrectly classified as non-cancerous but are actually cancerous. True positive (TP) represents cells correctly classified as cancer cells, and false positive (FP) refers to cells incorrectly identified as cancerous but not actually non-cancerous. Overall, our method achieved an accuracy rate of 80% despite single-cell variation in shape, size, and position in the cell cycle.

A clinical tumor sample contains both cancer and non-cancerous cells, even if it is malignant. The percentage of cancer cells varies according to the stage of tumor development. Here, we set a cancer risk level classification to low risk, medium risk, or high risk on the basis of the cancer cell percentile in a tumor biopsy. Figure 3d shows the diagnostic protocol and evaluation criteria. Tumor cells obtained from the tumor and non-cancerous cells from the region outside the tumor passed through the IC-ECIS for single-cell impedance measurement. The upper impedance limit of all cells from the non-tumor sample is set as the threshold. The risk level is based on the proportion of tumor cells that exceed the threshold, which are most likely to be cancer cells. When the proportion is <20%, the risk of the tested tumor being cancer is low, as it may come from the error of the impedance sensing system. When more than 40% of the cell impedance is abnormal, we consider it to be high risk. When the proportion is between 20% and 40%, we consider it to be a medium risk, in which case the doctors need to consider clinical symptoms for a more precise judgment. The 20% threshold is derived from the accuracy of our IC-ECIS method, which is 80% in distinguishing between normal cells and cancer cells. Thus, a 20% margin of error is within the acceptable range. The 40% (double of error range) was chosen as the high-risk cancer threshold, which is not fixed. As sample sizes and tumor types increase, the threshold will be adjusted to better suit different cancer types.

The processing time of a diagnosis method is critical for decision-making during the surgical operation. The turnaround time of a sample on the IC-ECIS platform is limited by tumor dissociation into single cells. To validate the shortest time to obtain enough primary tumor cells for IC-ECIS, we collected three tumor specimens from the same patient and systematically assessed their dissociation rates. The sizes of the samples varied from 0.13 cm^3 to 0.78 cm^3 to 3.11 cm^3. As shown in Fig. 3e, while larger tumor samples yielded more cells within the same time frame because the larger surface area contacted the tumor digestion buffer, they required a longer time to complete the dissociation process. Notably, even the smallest sample yielded over 3000 single cells within 15 min, a quantity sufficient for subsequent on-chip detection. The whole diagnostic process, including impedance measurement, can be accomplished in 20 min. Compared with the 1-h turnaround time for frozen pathology[12], a 20-min tumor diagnosis based on IC-ECIS has the potential for the doctor to determine whether to expand the dissection area during surgery.

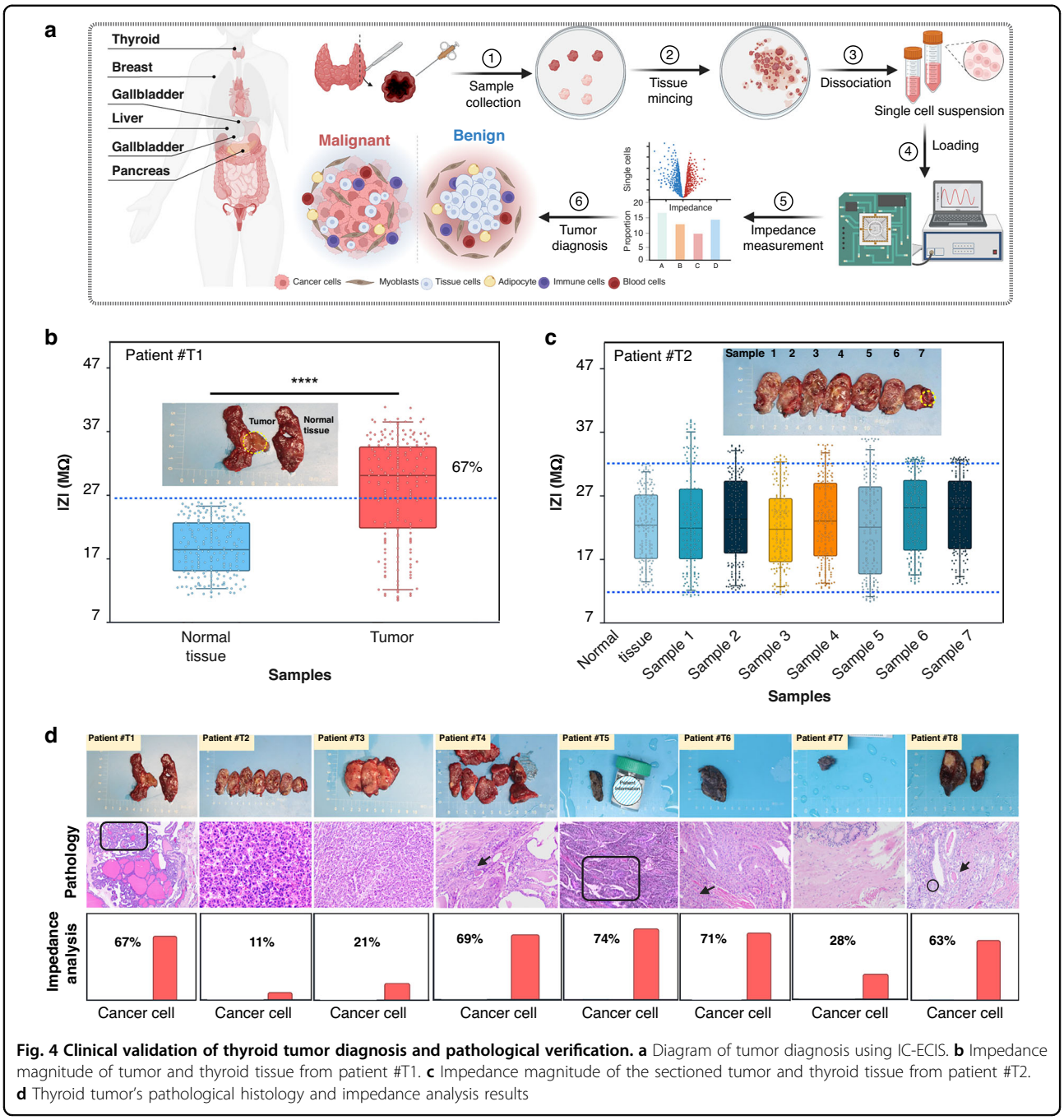

Fig. 4 Clinical validation of thyroid tumor diagnosis and pathological verification. a Diagram of tumor diagnosis using IC-ECIS. **b** Impedance magnitude of tumor and thyroid tissue from patient #T1. **c** Impedance magnitude of the sectioned tumor and thyroid tissue from patient #T2. **d** Thyroid tumor's pathological histology and impedance analysis results

Thyroid tumor diagnosis

To validate our tumor diagnosis criterion on the IC-ECIS platform, we conducted impedance analysis on clinical tumor samples and marked their cancer risk levels. Thyroid tumors, which are commonly found in the neck, often present as painless nodules, making distinguishing between benign and malignant tumors based on symptoms alone difficult. The preoperative misdiagnosis rate is high for thyroid tumors[47]. Here, we used thyroid tumor samples to preliminarily validate our IC-ECIS for tumor diagnosis by comparing the results with those of traditional tissue staining techniques.

Figure 4a shows the procedure for assessing primary tumors. The process involved surgical removal of the tumor, followed by the extraction of samples from various locations using biopsy needles. Normal tissues away from the tumor region were also collected as controls. These tissues were then dissociated into single cells and placed onto IC-ECIS chips. Cells whose impedance was higher than the upper impedance limit of cells from normal

tissue were considered cancer cells. The cancer cell percentile in a tumor was determined based on impedance measurements, allowing us to characterize the tumor.

Figure 4b shows an example of impedance magnitude measurements from cells sourced from both normal thyroid tissue and tumor tissue from Patient #T1, a highly suspicious thyroid cancer patient according to conventional preoperative diagnosis. The cells from the tumor exhibited higher impedance magnitudes than the cells from surrounding normal tissues, indicating that most of the tumor cells were cancerous. With the threshold of the upper limit of normal cell impedance (27 MΩ), 67% of the cells from the tumor were cancer cells, indicating a high risk of cancer. Figure 4c shows another example from Patient #T2. The percentage of cancer cells at various locations in the tumor was tested. As demonstrated, no obvious difference was observed between the tumor cells and normal cells. Only 11% of the tumor cells were identified as cancer cells. On the basis of the IC-ECIS criterion, this tumor was highly likely benign. More tumor testing results and histological pathology images are shown in Fig. 4d. Patients #T1, T4, T5, T6 and T8 had more than 40% cancer cells (high risk). Patient #T2 had 11% cancer cells, which was lower than 20% (low risk). Patients #T3, T7 had cancer percentages between 20% and 40% (medium risk).

We compared the tumor diagnosis based on IC-ECIS with the preoperative diagnosis based on various imaging techniques and the gold standard diagnosis with pathological analysis. As shown in Table 1, our diagnostic results were completely consistent with the gold standard pathological diagnosis at collaborating hospitals via the traditional hematoxylin-eosin (HE) staining method. Histopathological images are shown in Fig. 4d. For the IC-ECIS patients diagnosed at high risk levels (T1, T4, T5, T6, and T8), the pathological results revealed papillary thyroid carcinoma. Histopathological images revealed irregular cellular structures, including variations in cell size (black circles), elongation (black arrows), and papillary features (black square), indicative of cancerous cell morphology. For the IC-ECIS-diagnosed low-risk (T2) patients, the pathological results revealed nodules, whereas the medium-risk (T3 and T7) patients presented with papillary follicular adenoma. The histological features were consistent with those of normal healthy cells and were characterized by uniform cell morphology, singular spheroid nuclei, and finely distributed chromatin. Notably, T4. Its preoperative diagnosis showed C-TIRADS 4a, which is a suspicious cancer with a 5–15% chance of malignancy[48]. However, the pathological results revealed papillary thyroid carcinoma, ruling out prediagnosis. For this case, our diagnosis, which was based on the IC-ECIS criterion, was high risk, which was consistent with the gold standard approach and demonstrated its

Table 1 Tumor diagnosis with various methods

	Patient #	Tumor morphology	Preoperative diagnosis	Risk level (on-chip)	Pathological result
Thyroid	T1	Maximum diameter is 2 cm	C-TIRADS 4c	High	Papillary thyroid carcinoma
	T2	5.5 cm × 4 cm × 2.5 cm, soft, partially grayish white	C-TIRADS 4a	Low	Nodules
	T3	3.8 cm × 3.3 cm ×3.1 cm, soft, partially grayish white	C-TIRADS 4b	Medium	Thyroid follicular adenoma
	T4	Maximum diameter is 0.7 cm, and some areas are calcified	C-TIRADS 4a	High	Papillary thyroid carcinoma
	T5	Maximum diameter is 0.8 cm, gray tissue, hard	C-TIRADS 4c	High	Papillary thyroid carcinoma
	T6	Maximum diameter is 1.0 cm, and gray-red tissue	C-TIRADS 4c	High	Papillary thyroid carcinoma
	T7	Maximum diameter is 0.3 cm, hard	C-TIRADS 4b	Medium	Thyroid follicular adenoma
	T8	Maximum diameter is 1.5 cm, gray tissue, hard	C-TIRADS 4b	High	Papillary thyroid carcinoma
Liver	L1	7.5 cm × 6.5 cm ×6 cm, soft, gray-yellow tumor	\	High	Liver cancer
	L2	Multiple tumors, the largest diameter is 11 cm	cT3N0M0 Stage II	High	Liver cancer
Cholangiocarcinoma	C1	Maximum diameter is 4.5 cm, hard, white tumor	\	High	Cholangiocarcinoma
Breast	B1	6 cm × 5 cm × 3.5 cm, gray-yellow tissue	BI-RADS 4b	High	Invasive breast cancer
Gallbladder	G1	Maximum diameter is 6 cm, gray-yellow tissue	\	High	Gallbladder cancer
Pancreatic	P1	Maximum diameter is 2.6 cm, gray-white tissue	\	High	Pancreatic cancer

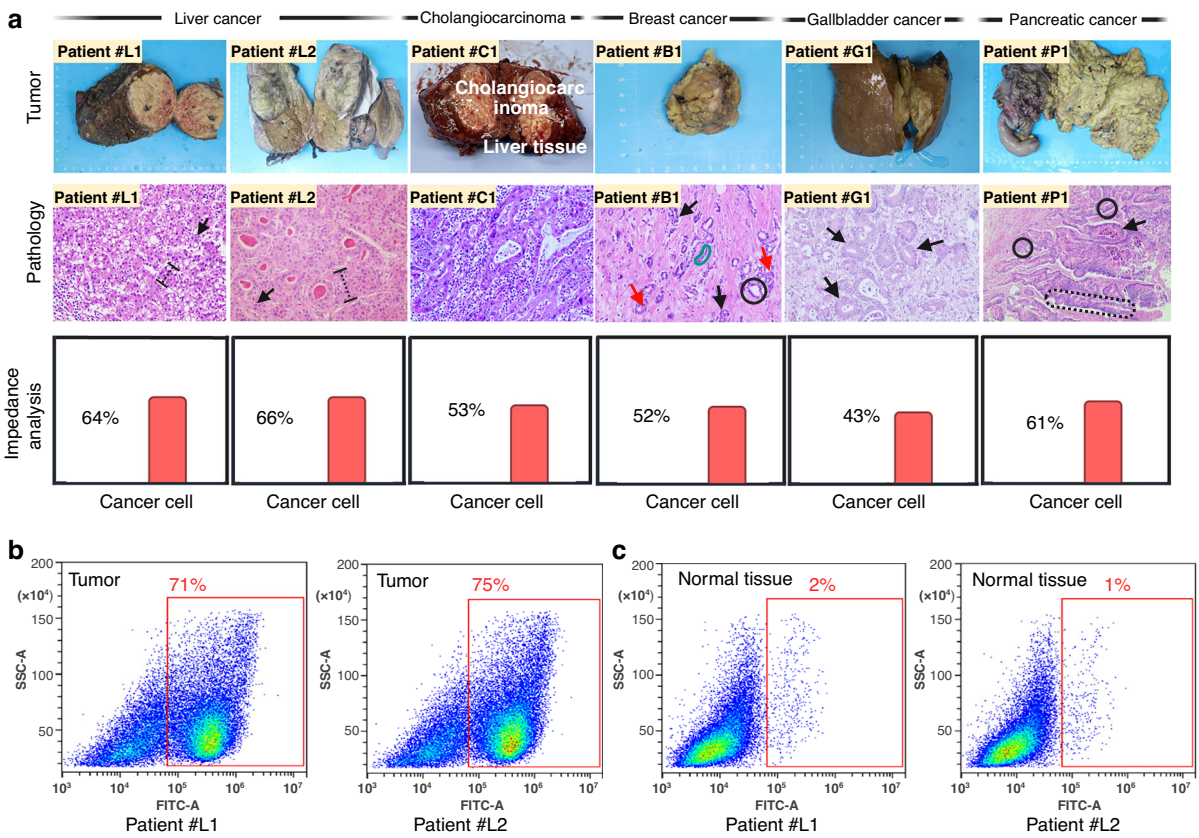

Fig. 5 Clinical validation of tumor diagnosis and pathological verification for liver, gallbladder, bile duct, breast, and pancreas. **a** Pathological results and impedance analysis results. **b** Flow cytometry results for tumor tissue from patients #L1 and #L2. **c** Flow cytometry results for normal tissue from patients #L1 and #L2

accuracy. The 20-min turnaround time supported the fast and accurate intraoperative diagnosis of thyroid cancer.

Application in other tumor diagnoses

To assess the general applicability of tumor malignancy diagnosis via IC-ECIS, we tested the method on other tumors from the liver (L1, L2), bile duct (C1), breast (B1), gallbladder (G1), and pancreas (P1).

Figure 5a shows the tumor images, the histological images, and the proportion of abnormal cells in the IC-ECIS. For the microscopic pathology samples of patients L1 and L2, the trabecular architecture in the tumor tissue was broader, with many areas of two or more thick cells (dotted line) and prominent nucleoli (black arrows) indicative of a malignant tumor. The biopsy of patient B1 revealed mostly single-layer cells in the breast ducts (green shape), some irregular nests of cells (black arrows), visible tubular formations (black circle), and increased nuclear-cytoplasmic (NC) ratios (red arrows). These features are compatible with invasive ductal carcinoma. For patient G1, variable-sized glands (black arrows) that infiltrate the wall of the gallbladder. The glands are surrounded by a desmoplastic stroma. In general, these findings suggested adenocarcinoma of the gallbladder. For patient P1, we observed predominantly a complex arborizing papillary architecture (black arrow), high-grade dysplasia (dashed shape), and enlarged, irregular nuclei (black circle) predominantly. These observations were consistent with those in pancreatic ductal adenocarcinoma. The histological images clearly revealed cancerous cells, confirming the malignancy of the tumors. Our IC-ECIS diagnosis revealed that more than 40% of the tumors were cancer cells, indicating a high risk of being malignant tumors.

To further validate the reliability of the impedance sensing technique for determining the proportion of cancer cells, we compared our results with those obtained via flow cytometry. Two liver tumor samples (L1 and L2) and corresponding normal tissues were used as examples. The focus of this analysis was on glypican-3 (GPC-3), a crucial tumor marker associated with hepatocellular carcinoma[49]. As shown in Fig. 5b, 71% of the cells from sample L1 and 75% from sample L2 specifically bound to the antibody, indicating a high percentage of GPC-3-positive cells in the

tumor. These proportions were consistent with those obtained via the IC-ECIS method, which were 63% and 66%, respectively. The slight deviation may be attributed to differences in the cell cycle phases of the cancer cells. As well as the presence of GPC-3–positive subpopulations that exhibit weaker adhesion to the electrode surface and consequently lower impedance signals[50,51]. In comparison, only 2% and 1% of the cells from normal tissue bound to the antibodies, as shown in Fig. 5c. This was likely due to non-specific binding or incidental expression, which are considered acceptable background values in flow cytometry.

The tumor diagnosis results are summarized in Table 1. The risk levels based on the IC-ECIS were all high, showing good consistency with the available preoperative diagnosis and the gold standard pathological diagnosis after surgical operation. This consistency highlights the accuracy of our method. Given the short turnaround time of IC-ECIS, it has the potential to be used during surgery for fast diagnosis, which will aid surgeons in deciding whether to broaden the dissection area.

Conclusion

Timely and accurate tumor diagnosis is critical for optimizing surgical outcomes and improving patient prognosis. In this study, we present a fast, accurate, automated, and easy-to-operate method based on IC-ECIS at the single-cell level for differentiating benign and malignant tumors. The advantage of the proposed method lies in the tight integration of ECIS with IC technology, which significantly shortens the signal path and effectively suppresses parasitic capacitance and external noise. The turnaround time of a sample can be as short as 20 min, enabling it to be used during the operation. The incorporation of the P-eSiFO chip processing technique has substantially decreased production costs and time, making disposable diagnostic chips viable for clinical use. The platform's efficacy was confirmed through small samples of clinical trials involving a variety of tumor samples, demonstrating its ability to match traditional pathology results in distinguishing benign from malignant tumors.

However, the IC-ECIS platform also has some limitations. 1) The low replication of cell positions on each electrode in large-scale applications. We are currently developing dielectrophoretic technology to move individual cells to the center of the electrodes precisely, and we will report the results elsewhere. 2) Integrating IC technology into clinical diagnosis may involve high costs. We will reduce costs through batch production and large-scale production. 3) Long-term cell culture and monitoring on IC chips can affect cell viability. Future research will adopt surface modification strategies to reduce cell damage and improve the interaction between cells and electrodes.

This advancement offers a scalable and cost-efficient solution to aid surgical decision-making and precision medicine. By connecting advanced technology with real-world clinical needs, this innovation paves the way for the widespread implementation of fast tumor diagnostic tools, thereby improving the quality of cancer care. The FPGA-based architectures are naturally well-suited for image preprocessing, feature extraction, and the integration of image-derived features with single-cell impedance signals, providing a scalable hardware foundation for multimodal intraoperative diagnosis. In the future, our platform can combine frozen pathology and AI to greatly improve the accuracy of fast intraoperative diagnosis of tumors.

Acknowledgements

We thank the technical and administrative team of the State-Key Laboratory of Analog and Mixed-Signal VLSI at the University of Macau for all their support.

Author details

[1]State Key Laboratory of Analog and Mixed-Signal VLSI, Institute of Microelectronics, University of Macau, Macau, SAR, China. [2]Faculty of Science and Technology, University of Macau, Macau, SAR, China. [3]Zhuhai ProMed Precision Medical Technology Co., Ltd, Zhuhai, China. [4]School of Integrated Circuits, Peking University, Beijing, China. [5]Faculty of Health Sciences, University of Macau, Macau, SAR, China. [6]Department of Hepatobiliary Surgery, First Affiliated Hospital of Guangzhou Medical University, Guangzhou, China. [7]Liver Transplantation Center, Third Affiliated Hospital, Sun Yat-Sen University, Guangzhou, China. [8]Southeast University, School of Integrated Circuits, Key Laboratory of MEMS of Ministry of Education, Wuxi, China. [9]Department of Laboratory Medicine, Sichuan Provincial People's Hospital, School of Medicine, University of Electronic Science and Technology of China, Chengdu, Sichuan, China. [10]Guangdong ACXEL Micro & Nano Tech Co., Ltd., Foshan, China. [11]On leave from Instituto Superior Tecnico, Universidade de Lisboa, Lisboa, Portugal. [12]MoE Frontiers Science Center for Precision Oncology, University of Macau, Macau, SAR, China

Author contributions

Y.J., W.H., and W.W. conceived this project. Y.J., K.L., P.M., and R.M. funded this project. W.H. performed experiments on clinical samples. K.L. and W.H. designed the hardware and software. Y.Z. P.W., S.Y., and X.H. helped in experiments in clinical sample preparation and data collection. W.H., Y.J., H.M., and L.C. prepared the manuscript.

Funding

This work is supported by the Macau Science and Technology Development Fund (FDCT) [FDCT0168/2023/RIA3, FDCT0001/2025/RID, FDCT0213/2024/AGJ, FDCT0001/2025/NRP]; University of Macau [MYRG-GRG2023-00092-IME, UMDF-TISF/2025/014/IME]. Guangdong Scientific and Technological Project (2025A0505010003).

Conflict of interest

The authors declare no competing interests.

Ethical declaration statement

The clinical samples are from the Third Affiliated Hospital of Sun Yat-Sen University and First Affiliated Hospital of Guangzhou Medical University. This study was approved by the Research Ethics Board of the University of Macau (Protocol # BRSERE23-APP009-IME as supporting information), and all participating patients provided informed consent prior to surgery. Immediately following surgery, clinical specimens were obtained from excised tissue.

Supplementary information The online version contains supplementary material available at https://doi.org/10.1038/s41378-026-01229-w.

Received: 28 November 2025 Revised: 26 January 2026 Accepted: 9 February 2026
Published online: 12 May 2026

References

1. Srivastava, S. et al. Cancer overdiagnosis: a biological challenge and clinical dilemma. *Nat. Rev. Cancer* **19**, 349–358 (2019).
2. Fitzgerald, R. C., Antoniou, A. C., Fruk, L. & Rosenfeld, N. The future of early cancer detection. *Nat. Med.* **28**, 666–677 (2022).
3. Shmatko, A., Ghaffari Laleh, N., Gerstung, M. & Kather, J. N. Artificial intelligence in histopathology: enhancing cancer research and clinical oncology. *Nat. Cancer* **3**, 1026–1038 (2022).
4. Pruessmann, W. et al. Molecular analysis of primary melanoma T cells identifies patients at risk for metastatic recurrence. *Nat. Cancer* **1**, 197–209 (2020).
5. Link, J. M. et al. Ongoing replication stress tolerance and clonal T cell responses distinguish liver and lung recurrence and outcomes in pancreatic cancer. *Nat. Cancer* **6**, 123–144 (2025).
6. Mu, W. et al. Non-invasive decision support for NSCLC treatment using PET/CT radiomics. *Nat. Commun.* **11**, 5228 (2020).
7. Zhong, Y. et al. PET/CT based cross-modal deep learning signature to predict occult nodal metastasis in lung cancer. *Nat. Commun.* **14**, 7513 (2023).
8. Borrelli, P. et al. AI-based detection of lung lesions in [18F] FDG PET-CT from lung cancer patients. *EJNMMI Phys.* **8**, 32 (2021).
9. Van Allen, E. M. et al. Whole-exome sequencing and clinical interpretation of formalin-fixed, paraffin-embedded tumor samples to guide precision cancer medicine. *Nat. Med.* **20**, 682–688 (2014).
10. Cruz-Flores, R., López-Carvallo, J. A., Cáceres-Martínez, J. & Dhar, A. K. Microbiome analysis from formalin-fixed paraffin-embedded tissues: current challenges and future perspectives. *J. Microbiol. Methods* **196**, 106476 (2022).
11. Weber, W. P. et al. Accuracy of frozen section analysis versus specimen radiography during breast-conserving surgery for nonpalpable lesions. *World J. Surg.* **32**, 2599–2606 (2008).
12. Akbarzadeh-Jahromi, M., Aslani, F. S., Raeisi, H., Momtahan, M. & Taheri, N. Comparison of frozen and permanent section diagnosis in ovarian neoplasms: analysis of factors affecting accuracy. *Int. J. Gynecol. Pathol.* **41**, 327–336 (2022).
13. Cicek, M. T. et al. The impact of the frozen section analysis on surgical strategy in nodular thyroid diseases. *Med. Sci.* **10**, 794–798 (2021).
14. Barlogie, B. et al. Flow cytometry in clinical cancer research. *Cancer Res.* **43**, 3982–3997 (1983).
15. Meda, B. A. et al. Diagnosis and subclassification of primary and recurrent lymphoma: the usefulness and limitations of combined fine-needle aspiration cytomorphology and flow cytometry. *Am. J. Clin. Pathol.* **113**, 688–699 (2000).
16. Robertson, S., Azizpour, H., Smith, K. & Hartman, J. Digital image analysis in breast pathology—from image processing techniques to artificial intelligence. *Transl. Res.* **194**, 19–35 (2018).
17. Bakrania, A., Joshi, N., Zhao, X., Zheng, G. & Bhat, M. Artificial intelligence in liver cancers: Decoding the impact of machine learning models in clinical diagnosis of primary liver cancers and liver cancer metastases. *Pharmacol. Res.* **189**, 106706 (2023).
18. Wijsman, P. C. et al. Detection of airway remodeling in asthma using bronchoscopic optical coherence tomography. *CHEST Pulmonary* **3**, 100143 (2025).
19. Zeppieri, M. et al. Optical coherence tomography (OCT): a brief look at the uses and technological evolution of ophthalmology. *Medicina* **59**, 2114 (2023).
20. Orringer, D. A. et al. Rapid intraoperative histology of unprocessed surgical specimens via fibre-laser-based stimulated Raman scattering microscopy. *Nat. Biomed. Eng.* **1**, 0027 (2017).
21. Zhang, J. et al. Nondestructive tissue analysis for ex vivo and in vivo cancer diagnosis using a handheld mass spectrometry system. *Sci. Transl. Med.* **9**, eaan3968 (2017).
22. Balog, J. et al. Intraoperative tissue identification using rapid evaporative ionization mass spectrometry. *Sci. Transl. Med.* **5**, 194ra193–194ra193 (2013).
23. Van Hese, L. et al. The diagnostic accuracy of intraoperative differentiation and delineation techniques in brain tumours. *Discov. Oncol.* **13**, 123 (2022).
24. Ngoc Le, H. T., Kim, J., Park, J. & Cho, S. A review of electrical impedance characterization of cells for label-free and real-time assays. *BioChip J.* **13**, 295–305 (2019).
25. Srinivasaraghavan, V. Bioimpedance spectroscopy of breast cancer cells: a microsystems approach. PhD thesis, Virginia Tech (2015).
26. Wegener, J., Keese, C. R. & Giaever, I. Electric cell–substrate impedance sensing (ECIS) as a noninvasive means to monitor the kinetics of cell spreading to artificial surfaces. *Exp. Cell Res.* **259**, 158–166 (2000).
27. Zhang, Z. et al. Recent advances in electrical impedance sensing technology for single-cell analysis. *Biosensors* **11**, 470 (2021).
28. Arya, S. K., Lee, K. C., Dah'alan, D.uB. & Rahman, A. R. A. Breast tumor cell detection at single cell resolution using an electrochemical impedance technique. *Lab a Chip* **12**, 2362–2368 (2012).
29. Gelsinger, M. L., Tupper, L. L. & Matteson, D. S. Cell line classification using electric cell-substrate impedance sensing (ECIS). *Int. J. Biostatistics* **16**, 20180083 (2020).
30. Reyntjens, S. & Puers, R. A review of focused ion beam applications in microsystemtechnology. *J. Micromech. Microeng.* **11**, 287 (2001).
31. Chen, L. et al. A polymer-based embedded silicon fan-out packaging (P-eSiFO) method for high-density chiplet packaging. *IEEE Trans. Compon., Packaging Manuf. Technol.* **13**, 1743–1749 (2023).
32. Chen, L., Zhang, B., Zhang, C. & Wang, W. In Proc. 2024 25th International Conference on Electronic Packaging Technology (ICEPT) 1–5 (IEEE, 2024).
33. Agnesina, A. et al. Power, performance, area, and cost analysis of face-to-face-bonded 3-D ICs. *IEEE Trans. Compon., Packaging Manuf. Technol.* **13**, 300–314 (2023).
34. Han, A., Yang, L. & Frazier, A. B. Quantification of the heterogeneity in breast cancer cell lines using whole-cell impedance spectroscopy. *Clin. Cancer Res.* **13**, 139–143 (2007).
35. Wang, Y., Xia, Y. & Lu, Z. Metabolic features of cancer cells. *Cancer Commun.* **38**, 65 (2018).
36. Semenza, G. L. Tumor metabolism: cancer cells give and take lactate. *J. Clin. Investig.* **118**, 3835–3837 (2008).
37. Szachowicz-Petelska, B., Dobrzynska, I., Sulkowski, S., Figaszewski, Z. A. & Ettarh, R. Characterization of the cell membrane during cancer transformation. In *Cancer Biology – From Genes to Tumor* (ed. Ettarh, R.) 241–256 (InTech, 2012).
38. Vander Heiden, M. G., Cantley, L. C. & Thompson, C. B. Understanding the Warburg effect: the metabolic requirements of cell proliferation. *science* **324**, 1029–1033 (2009).
39. Behari, J., Alex, Z. & Zaidi, Z. H. Dielectric permittivity of biological tissues in the microwave frequency range. *In Advanced Microwave and Millimeter-Wave Detectors* (eds. Sato, S. S. & Behari, J.) **2275**, 301–308 (SPIE, 1994).
40. Behrens, J. The role of cell adhesion molecules in cancer invasion and metastasis. *Breast Cancer Res. Treat.* **24**, 175–184 (1993).
41. Mareel, M. & Leroy, A. Clinical, cellular, and molecular aspects of cancer invasion. *Physiol. Rev.* **83**, 337–376 (2003).
42. Giaever, I. & Keese, C. R. Monitoring fibroblast behavior in tissue culture with an applied electric field. *Proc. Natl. Acad. Sci.* **81**, 3761–3764 (1984).
43. Montoya, M. C., Sancho, D., Vicente-Manzanares, M. & Sánchez-Madrid, F. Cell adhesion and polarity during immune interactions. *Immunol. Rev.* **186**, 68–82 (2002).
44. Holmes, D. et al. Leukocyte analysis and differentiation using high speed microfluidic single cell impedance cytometry. *Lab a Chip* **9**, 2881–2889 (2009).
45. Augello, A. & De Bari, C. The regulation of differentiation in mesenchymal stem cells. *Hum. Gene Ther.* **21**, 1226–1238 (2010).
46. Cook, D. & Genever, P. Regulation of mesenchymal stem cell differentiation. *Adv. Exp. Med. Biol.* **789**, 213–229 (2013).
47. Vargas, N. R., Matos, M. & Kinaan, M. Hidden in plain sight: incidental diagnosis of metastatic papillary thyroid microcarcinoma without radiologically apparent thyroid tumor. *AACE Clin. Case Rep.* **11**, 58–61 (2025).
48. Chen, Q., Lin, M. & Wu, S. Validating and comparing C-TIRADS, K-TIRADS and ACR-TIRADS in stratifying the malignancy risk of thyroid nodules. *Front. Endocrinol.* **13**, 899575 (2022).
49. Wang, L., Yao, M., Pan, L.-H., Qian, Q. & Yao, D.-F. Glypican-3 is a biomarker and a therapeutic target of hepatocellular carcinoma. *Hepatobiliary Pancreat. Dis. Int.* **14**, 361–366 (2015).
50. Hamaoka, M., Kobayashi, T., Tanaka, Y., Mashima, H. & Ohdan, H. Clinical significance of glypican-3-positive circulating tumor cells of hepatocellular carcinoma patients: a prospective study. *PLoS One* **14**, e0217586 (2019).
51. Wu, Y. et al. Glypican-3 promotes epithelial-mesenchymal transition of hepatocellular carcinoma cells through ERK signaling pathway. *Int. J. Oncol.* **46**, 1275–1285 (2015).